Low Temperature Physics/Fizika Nizkikh Temperatur, 2016, v. 42, No. 9, pp. 951–958

The annealing influence onto the electrical and magnetic behavior of magnetoresistive/insulator system

A.M. Ahmed, Abd El-Mo'ez A. Mohamed, H.F. Mohamed, A.K. Diab, Aml M. Mohamed, and A.E.A. Mazen

Physics department, Faculty of Science, Sohag University 82524, Sohag, Egypt
E-mail: fikry_99@yahoo.com; a.ahmed@science.sohag.edu.eg

Received November 20, 2015, revised March 28, 2016, published online July 25, 2016

This investigation is mainly concerned with the effect of annealing temperature (600, 700, 800 and 900 °C) in air for $(La_{0.7}Ba_{0.3}MnO_3)_{1-x}/(NiO)_x$ with $x = 0$ and $x = 0.10$ samples. It was shown that the annealing temperature does not affect the structure and parameters of rhombohedral lattice of the samples. However, it is observed that the annealing treatment has a notable effect on the electrical resistivity and the metal-semiconductor transition temperature T_{ms}. Temperature dependent magnetization measurements showed a decrease in Curie temperature T_C with annealing temperature. In the same time, annealing process decreases the magnetoresistance of $La_{0.7}Ba_{0.3}MnO_3$, in contrast to $(La_{0.7}Ba_{0.3}MnO_3)_{0.9}/(NiO)_{0.1}$ composite.

PACS: 75.47.Lx Magnetic oxides;
75.47.Gk Colossal magnetoresistance;
72.80.Tm Composite materials.

Keywords: colossal magnetoresistance; electrical resistivity; magnetization

Magnetoresistive rare earth doped manganites $A_{1-x}B_xMnO_3$, where A is a rare earth element and B is a divalent ion, are known with its fantastic properties as electrical resistivity suppression under magnetic field application [1] known as colossal magnetoresistance (CMR) which open the gate for the participation in potential applications [2]. In these materials, the double exchange (DE) is responsible for ferromagnetism and metalicity below transition temperature T_{ms}, where Mn^{3+} and Mn^{4+} ions are the heart of DE that can be controlled by changing doping level [3] or by oxygen stoichiometry [4]. Another systems based on manganites have received some attention are the magnetoresistive/insulator systems such as $La_{0.7}Sr_{0.3}MnO_3/CeO_2$ [5].

The magnetoresistive material was mixed with an insulator material to enhance the extrinsic CMR that depending on grain boundaries [6] and spin tunneling [7], that CMR may increase under low magnetic fields known as low field magnetoresistance (LFMR). The importance of LFMR refers to use low magnetic field to get high values of MR what is making it useful for applications. This LFMR can be affected by other several factors; one of them is annealing temperature that can affect the grain size and hence the physical properties including LFMR. An annealing effect has a little attention in this direction, especially in LBMO/insulator. Therefore in this work the effects of annealing temperature on the electrical, magnetic, magnetoresistance and thermoelectric properties of $La_{0.7}Ba_{0.3}MnO_3$ (LBMO) and $(La_{0.7}Ba_{0.3}MnO_3)_{0.9}/(NiO)_{0.1}$ (LBMO/NiO) are examined.

2. Experimental

$(La_{0.7}Ba_{0.3}MnO_3)_{1-x}/(NiO)_x$ ceramic samples were prepared by the conventional solid state reaction method ($x =$ = 0.0 & 0.10). La_2O_3, $BaCO_3$ and $MnCO_3$ raw materials were mixed in stoichiometric proportions, ground, pelletized and calcined at 900 °C for 24 h. It was reground again and pelletized and then sintered at 1100 °C for 24 h. NiO insulator was added in stoichiometric portions to the sintered $La_{0.7}Ba_{0.3}MnO_3$ compound and lightly ground, then pressed and put in 1000 °C for 24 h. The composites of LBMO and LBMO/NiO annealed for 2 h at 600, 700, 800 and 900 °C. Electrical resistivity was measured by van der Pauw technique in the presence and absence of 0.6 T magnetic field. Samples were examined by x ray, using Brucker (Axs-D& Advance) powder diffractometer at room temperature with Cu (K_α) radiation ($\lambda = 1.5406$ Å). The microstructure was investigated by Jeol JSM-6610LV

scanning electron microscope (SEM). The dc magnetization temperature dependence (Zero Field Cooled (ZFC)) were measured using an EV9 vibrating sample magnetometer (VSM) under 100 Oe in temperature range 100–400 K. The thermoelectric power measurements were carried out by means of a home-built set-up published in our previous works [8–10].

3. Results and discussion

3.1. Structure and SEM

Figures 1(a), (b) show XRD patterns of as-prepared and annealed samples of the two compositions (LBMO and LBMO/NiO). LBMO samples in Fig. 1(a) have single phase, while, LBMO/NiO samples in Fig. 1(b), have some additional peaks related to NiO insulator at 2θ = 37.25, 43.27, 62.879, 75.416 and 79.41° that do not affect by annealing process. In addition, there are small impurity peaks of La_2O_3 at 2θ ~ 26, 31.5 and 41°. The position of NiO phase peaks are in good agreement with Martin *et al*. [11].

Rietveld analysis patterns (Fig. 2(a), (b)) have proved the crystallization of two composites into rhombohedral structure (space group $R\bar{3}c$). From Fig. 2(b) we observe small impurities of La_2O_3 at 2θ ≈ 26, 31.5 and 41°. Fig. 2(b) confirms also the additional peaks related to NiO phase as was mentioned before. The cell parameters of all samples are unchanging (a = 5.5291, c = 13.4838Å). This means that the NiO does not react with LBMO matrix and act as insulator grains. The XRD results permitted to estimate the average crystallite size of the composite using Scherrer's equation, $\langle D\rangle = \frac{K\lambda}{\beta\cos\theta}$, where $\langle D\rangle$ is average particle size, K is a constant (shape factor of 0.89), λ is the Cu Kα wave length, and β is the full width at half maxima of the XRD peak. The crystallite sizes are found to be in the range of 34.68–40.72 and 24.542–27.286 nm of LBMO and LBMO/NiO respectively (Table 1).

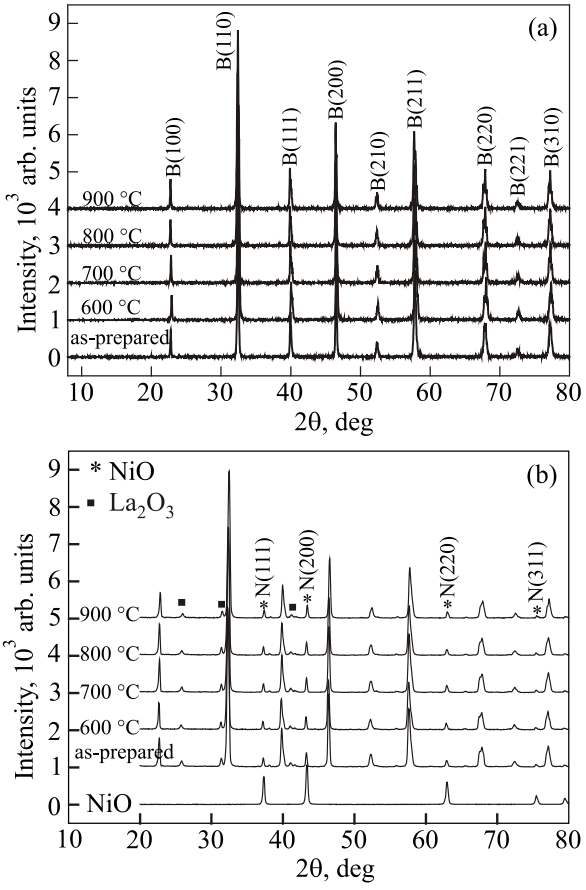

Fig. 1. XRD of the as-prepared and annealed samples of LBMO (a) and LBMO/NiO (b).

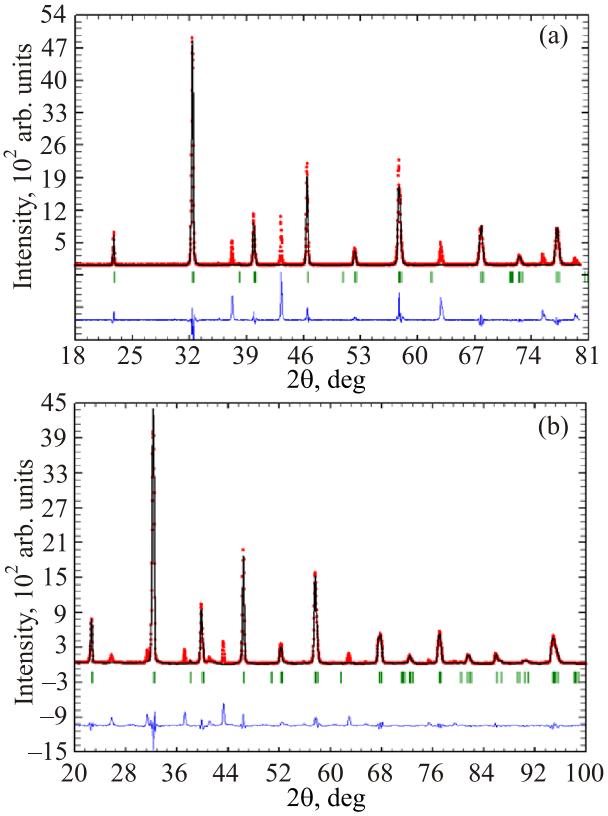

Fig. 2. (Color online) The reitveld based calculated profile at room temperature: LBMO (a), LBMO/NiO (b). The green marks indicate Bragg reflections, the red dots are the experimental data, black line is the theoretical calculations and the blue line is the difference between them.

Figure 3 exhibits surface morphology of samples by SEM, and shows the relatively enhancement of grain size in some annealing treatment. Grains have a sharp shape, increase un-sequential in size with annealing temperatures (as seen Table 1). The existence of all elements was confirmed by the energy dispersive x-ray analysis (EDAX) as seen in Fig. 4. Generally, the NiO peaks in XRD and SEM have emphasized the separated NiO phase which is the premise of spin valve formation. Noticeably, the grain sizes observed by SEM (μm range) area number of times larger than those calculated by XRD (nm range), which indicates that each grain observed by SEM consists of numerous crystallites. The change of grain size behaves as the variation of the average crystallite size $\langle D\rangle$ with differing values.

Table 1. The transition temperatures, T_{ms}, T_C and T_N and particle sizes SEM and $\langle D \rangle_{XRD}$ as function of annealing temperature of LBMO and LBMO/NiO

	Condition T, °C	T_{ms}, K	T_C, K	T_N, K	SEM, μm	$\langle D \rangle_{XRD}$, nm
$x = 0$	As-prepared	270	348	–	1.3	38.07
	600	284	335	–	1.29	35.29
	700	266	329	–	1.36	37.90
	800	258	317	–	1.37	40.72
	900	264	325	–	1.36	34.68
$x = 0.1$	As-prepared	180	321	367	0.673	25.104
	600	172	320	365	0.897	24.542
	700	176	315	362	0.742	25.897
	800	174	313	366	1.137	25.338
	900	174	320	364	0.973	27.286

3.2. Electrical properties

The temperature dependences of resistivity ρ (T) are shown in Fig. 5 for non-annealed and annealed samples (LBMO, LBMO/NiO). It is found that all samples have a metallic-semiconducting transition at certain temperature T_{ms}. The resistivity of the annealed LMBO sample decreases except for 800 °C (see Fig. 5(a)). Besides, T_{ms} decreases with increasing the annealing temperature starting at 700 °C (for LBMO) and at 600 °C (for LBMO/NiO). The resistivity and T_{ms} of the annealed LBMO/NiO samples are lower than those of as-prepared ones (see Fig. 5(b) and Table 1). The heat treatment has a weak effect on $T_{\rm ms}$. These effects can be attributed to the double exchange interactions (DE) between Mn^{3+}/Mn^{4+} ions. Furthermore, the Mn^{3+}/Mn^{4+} ratio to be affected by annealing process [12]. This is also supported by the change in DE and the resistivity drop in LBMO at annealing temperature T = = 600, 700 and 900 °C. Besides, oxygen vacancies can be a controlling parameter in the above two correlated factors [13], where the Mn^{3+}/Mn^{4+} ratio can be varied by the annealing process at different temperatures [14]. The annealing-generated oxygen vacancies in the LBMO can cause instability of the Ba ions agglomerating at LBMO grains. The Ba deficiency increases the Mn^{4+} contents and compensates the ratio lost by the oxygen vacancies, which decreases resistivity at 600, 700 and 900 °C. As for T = 800 °C, Ba agglomeration can intensify the carriers scattering and hence the resistivity increases. Moreover the very small size of the segregated Ba or the impurity phase perhaps is the reason why XRD cannot detect them [14].

The situation is different in LBMO/NiO due to the presence of NiO insulator interlaid LBMO grains. The annealing suppresses the Curie temperature and reduces T_{ms}.

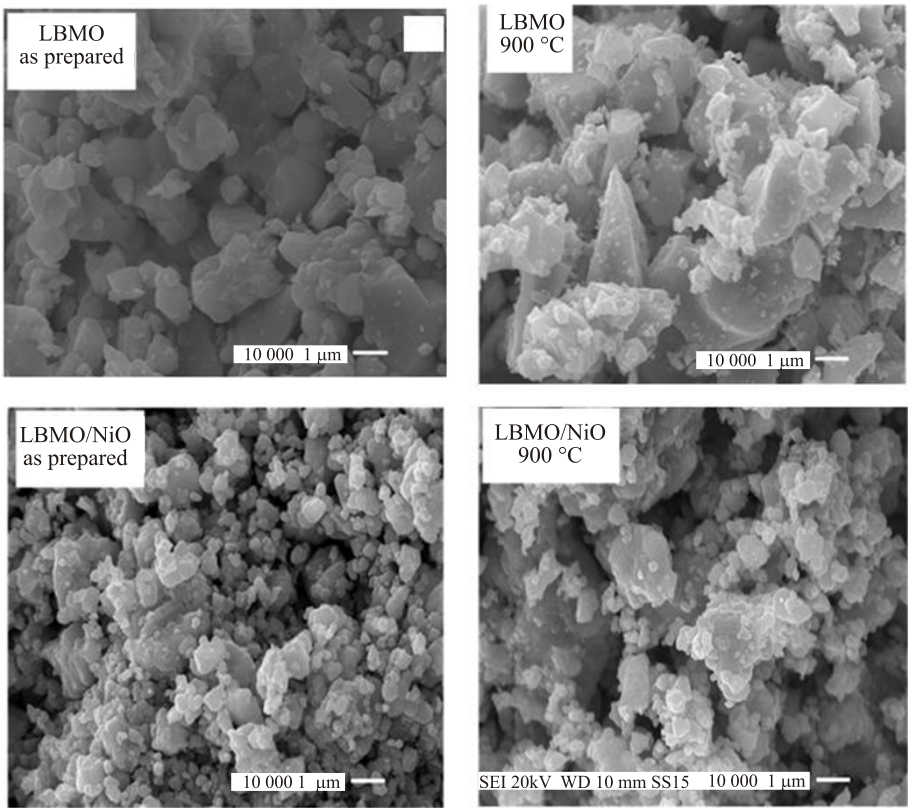

Fig. 3. SEM morphology of the as-prepared LBMO, LBMO/NiO and annealed samples.

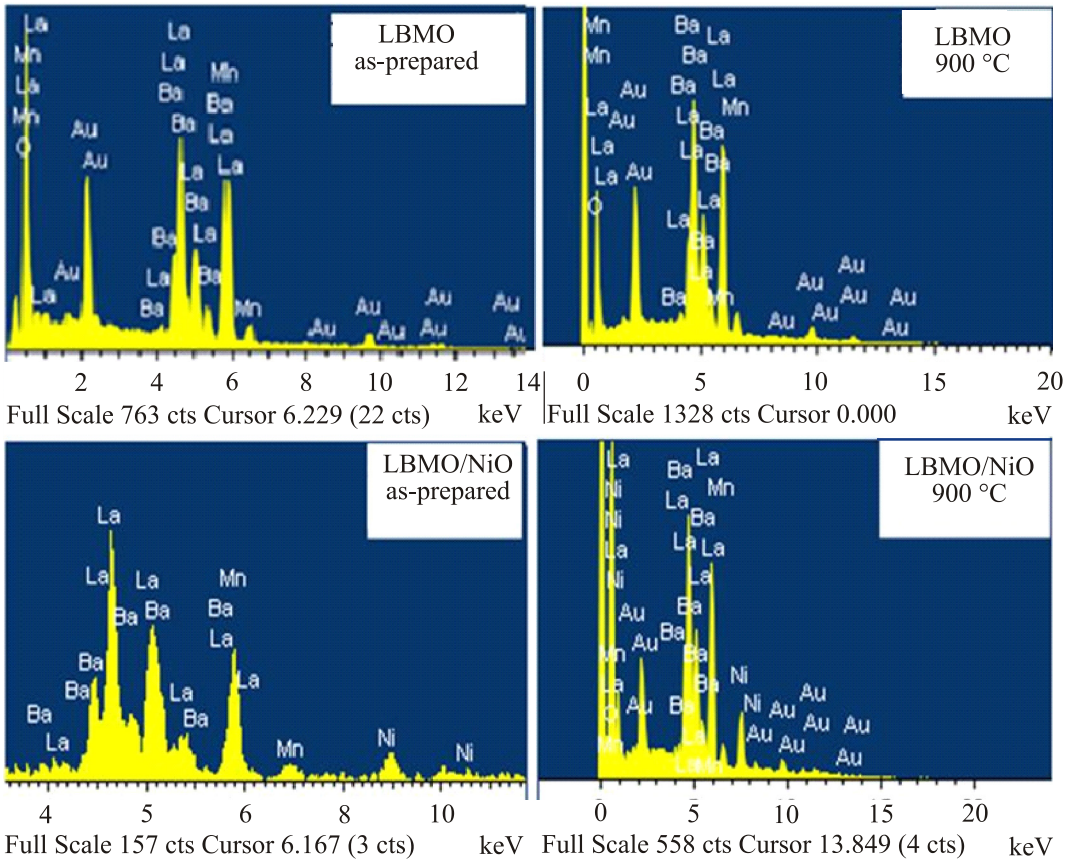

Fig. 4. EDX spectra of LBMO, LBMO/NiO and annealed samples.

The grain size plays an essential role in resistivity and T_{ms}, where the decreasing of these two quantities is related to bigger grain sizes. Following the model in Ref. 15 the grain has a core and an external shell. As the size of grains increases, its core volume increases, but the thickness of the shell decreases leading to the decrease of resistivity and T_{ms}. At annealing temperatures we can see grains of larger sizes. So, the intergrain connection should become better and resistivity reduces.

Since the Mn^{3+}–Mn^{4+} interaction is ferromagnetic, the transition to a ferromagnetic state enables the electron to hop between the Mn^{3+} and Mn^{4+} ions without spin flip. As a result the hopping resistance falls. The lowering temperature and the external magnetic field make spin flip even more difficult, which further decreases resistance.

3.3. Magnetoresistance

Magnetoresistance was calculated from the relation $[\rho(H)-\rho(0)]/\rho(0)$, where $\rho(H)$ is the resistivity measured in H = 0.6 T and $\rho(0)$ is the resistivity measured in zero magnetic field. The temperature dependence of magnetoresistance of the samples is shown in Fig. 6. There are small MR peaks for as-prepared and annealed LBMO (see Fig 6a). It is notable that the as-prepared sample has the highest MR values. As mentioned before (Sec. 3.2.), the deficiency increases the Mn^{4+} contents and compensates the ratio lost by oxygen vacancies. As a result, the tunneling resistivity decreases with annealing process (Fig. 5), and the applied magnetic field affects only the orientation of the magnetic moments of the grains and thus opens additional transport channels.

On the other hand, there is an appreciable enhancement of MR in LBMO/NiO at 600, 800 and 900 °C, especially at room temperature (290 K). The values of room temperature negative MR enhances from 1.96% for the as prepared sample to 18.42, 7.52 and 28.07% at 600, 800 and 900 °C, respectively (see Fig 6(b)). This may refer to the relatively small insulator grains (NiO) which have longer grain boundaries. This increases tunneling and hence MR.

3.4. Conduction mechanism

The $\rho(T)$ data for the semiconducting region were analyzed using the models of small polaron hopping (SPH) and the variable range hopping (VRH) existing in different temperature range [16,17]. According to SPH model [18], the resistivity changes as $\rho/T = \rho_\alpha \exp(E_P/k_BT)$ where ρ_α is a constant, E_ρ is the activation energy, k_B is the Boltzmann constant. This model is fitted with $\rho(T)$ at $T > \theta_D/2$ [19], where $\theta_D/2$ is the deviation from linearity of $\ln\rho/T$ vs. T^{-1} relation and θ_D is the Debye temperature. In VRH model the temperature dependence of conductivity described by expression $\sigma = \sigma_0 \exp(T_0/T)^{-1/4}$ [18] is well

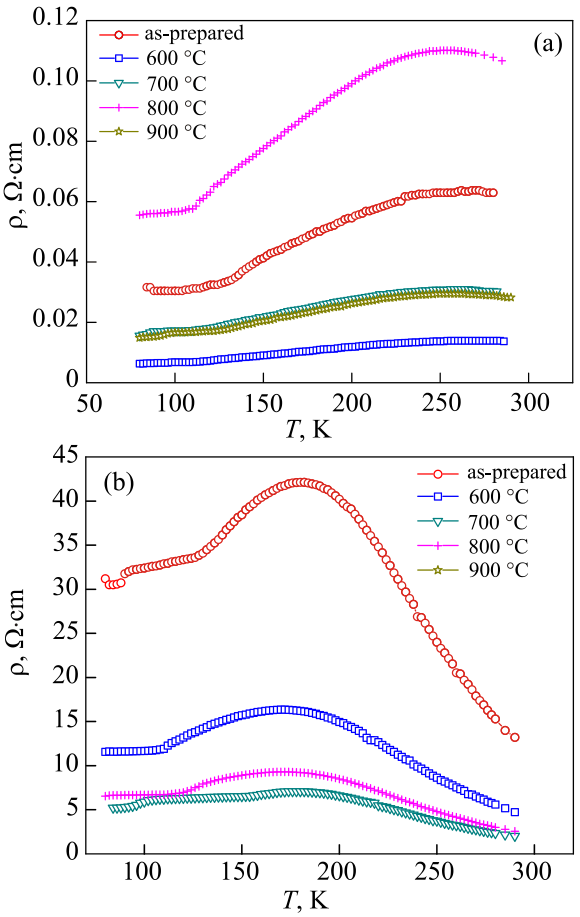

Fig. 5. (Color online) Temperature dependence resistivity of LBMO (a) and LBMO/NiO (b).

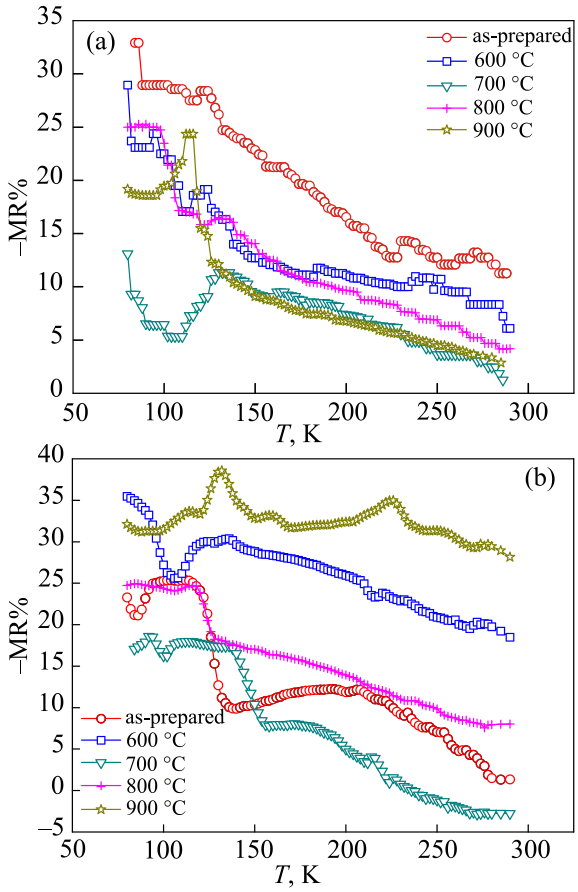

Fig. 6. (Color online) Temperature dependence MR (H = 0.6 T) of LBMO (a) and LBMO/NiO (b).

applicable at $T_{ms} < T < \theta_D/2$ [19]. $T_0 = 16a^3/k_B N(E_F)$ is the Mott characteristic temperature, $N(E_F)$ is the density of states near the Fermi energy and $1/a$ is the localization length $a = 2.22$ nm^{-1} as reported by Viret *et al.* [20].

The analysis of the data obtained within the two models shows that SPH and VRH conductions coexist in the as-prepared and annealed at 900 °C LBMO samples while SPH is the only dominant conduction mechanism at 600, 700 and 800 °C. In addition, θ_D and the optical phonon frequency ν_{ph} (calculated from the relation $h\nu_{ph} = k_B\theta_D$) decrease at 900 °C in comparison with the as-prepared LBMO sample (Table 2). For LBMO/NiO, SPH and VRH are present together in the as prepared and annealed samples, and the θ_D and ν_{ph} values are fluctuating with annealing temperatures (see Table 2). E_ρ, decreases with the annealing temperatures in both LBMO and LBMO/NiO,

Table 2. The calculated parameters, E_ρ, θ_D , ν_{ph}, W_{H_ρ}, γ_{ph} and $\exp(\gamma_{ph})$ as function of annealing temperature of LBMO and LBMO/NiO

	Condition T, °C	E_ρ, mev	θ_D, K	ν_{ph}	W_{H_ρ}, mev	γ_{ph}	$\exp\gamma_{ph}$
$x = 0$	As-prepared	79.20	572	$1.19\cdot10^{13}$	76.01	9.74	17000.5
	600	38.75	–	–	35.68	–	–
	700	32.90	–	–	19.06	–	–
	800	28.49	–	–	26.51	–	–
	900	37.01	548	$1.14\cdot10^{13}$	33.74	1.432	4.187
$x = 0.1$	As-prepared	121.92	500	$1.04\cdot10^{13}$	118.47	5.510	247.38
	600	121.28	504	$1.05\cdot10^{13}$	118.51	5.469	237.28
	700	116.68	488	$1.01\cdot10^{13}$	111.39	5.309	202.14
	800	116.93	484	$1\cdot10^{13}$	109.71	5.272	194.90
	900	115.46	487	$1.0\cdot10^{13}$	112.88	5.391	219.47

which may be due to the decrease in localization of e_g electron. This is resulting from the decrease in electron-phonon interaction γ_{ph} (see Table 2), as estimated from $\gamma_{ph} = 2W_H/h\nu_{ph}$ equation [18]. This effect seems strongly once the sample annealed at 600 °C, where E_ρ drop to half. The polaron hopping energy (W_H) also decreases with annealing temperatures, leading to increase of $N(E_F)$ and a decrease in resistivity. These electron-phonon interactions are rather strong because $\gamma_{ph} > 4$ [21]. On other hand, γ_{ph} is confirmed by the high values of $\exp(\gamma_{ph})$ (Table 2), describing the ratio between the polaron mass m_p and the effective rigid mass of the lattice m^* in the relation $m_P = m^* \exp(\gamma_{ph})$ [22].

To identify the type small polaron conduction whether it is an adiabatic or non-adiabatic process, we used Holstein criteria [23]:

$J > H$ for adiabatic condition,

$J < H$ for non-adiabatic condition,

where $J(T) \approx 0.67\, h\nu_{ph} \left(\frac{T}{\theta_D}\right)^{1/4}$

and $H = (2k_B T W_H/\pi)^{1/4}\ (h\nu_{ph}/\pi)^{1/2}$.

By using this criteria at $T = 290$ K, we found that the as-prepared LBMO has non-adiabatic conduction since $J < H$, and adiabatic conduction at 900 °C annealing temperature because $J > H$ (see Table 3). On contrary, the as-prepared LBMO/NiO has an adiabatic state under all annealing conditions as we say $J > H$, i.e., NiO holds the conduction state stability during annealing [24].

According to the VRH model, carriers can hop between the neighboring sites with the hopping energy (E_h) covering the hopping distance (R_h). Both E_h and R_h are the temperature dependent parameters determined at 290 K and calculated from the relations $E_h(T) = \frac{1}{4} k_B T^{3/4} T_0^{1/4}$ and $R_h(T) = \frac{3}{8} a (T_0/T)^{1/4}$ [25] respectively. As seen in Table 3, E_h and R_h decrease in the annealing process depending on the decrease of localization e_g electron and the decrease in γ_{ph} .

3.5. Magnetization

The temperature dependence of magnetization is shown in Figs. 7(a), (b). The curves $M_{zfc}(T)$, are for two compositions (H = 100 Oe). All the samples exhibit a ferromagnetic-paramagnetic transition at T_C, determined the minimum of its numerical first derivative, $dM(T)/dT$. The pure saturation and the sharp drop of magnetization in the parent LBMO support the high homogeneity of the samples in the XRD patterns, while the drop of LBMO/NiO is due to the existence of non-homogeneity NiO phase [26]. In the parent LBMO the annealing process increases magnetization and decreases T_C in agreement with $La_{1-x}Ce_xMnO_3$ [27]. As for the annealed LBMO sample at 900 °C, its higher T_C, may be due to an increase in Mn–O bond length which leads to the charge delocalization and promotes hopping of the electrons through the Mn–O–Mn path. This improves of the magnetization and expands the ferromagnetic region.

In the LBMO/NiO composite, there exists a ferro–paramagnetic phase transition at T_C. Also, the magnetization values approach those of the annealed samples. Moreover, all LBMN/NiO samples exhibit an antiferromagnetic (AFM) phase transition at Neel temperature T_N (see Table 1). The inset in Fig. 7(b) confirms this behavior (T_{an} = 800 °C), where the dependence dM/dT vs T has two peaks: the first one associates with the Curie temperature but the second one (higher T) refers to the Neel temperature. The appearance of the AFM phase is due to the segregation of the antiferromagnetic material NiO. This behavior of the LSMO/NiO composite was reported by Eshraghi *et al.* (2006) [28]. In addition the values of T_N of NiO close to the former study [29].

Table 3. The calculated parameters of hopping models, $N(E_f)$, J, H, $W_H/3$, R_h and E_h as function of annealing temperature of LBMO and LBMO/NiO

	Condition T, °C	$N(E_f)$, $eV^{-1}\cdot cm^3$	J, meV	H, meV	$W_H/3$, meV	R_h, Å	E_h, meV
$x = 0$	As-prepared	$6.12\cdot10^{24}$	27.80	23.06	25.34	1.79	6.66
	600	–	–	–	11.89	–	–
	700	–	–	–	6.35	–	–
	800	–	–	–	8.83	–	–
	900	$6.0\cdot10^{24}$	26.92	18.65	11.24	1.756	6.51
$x = 0.1$	As-prepared	$6.08\cdot10^{20}$	25.13	24.38	39.49	66.73	18
	600	$9.63\cdot10^{20}$	25.28	24.48	39.50	59.49	16.05
	700	$10.5\cdot10^{20}$	24.68	23.72	37.13	58.22	15.71
	800	$10\cdot10^{20}$	24.53	23.54	36.57	58.91	15.89
	900	$77\cdot10^{20}$	24.64	23.78	37.62	35.37	9.54

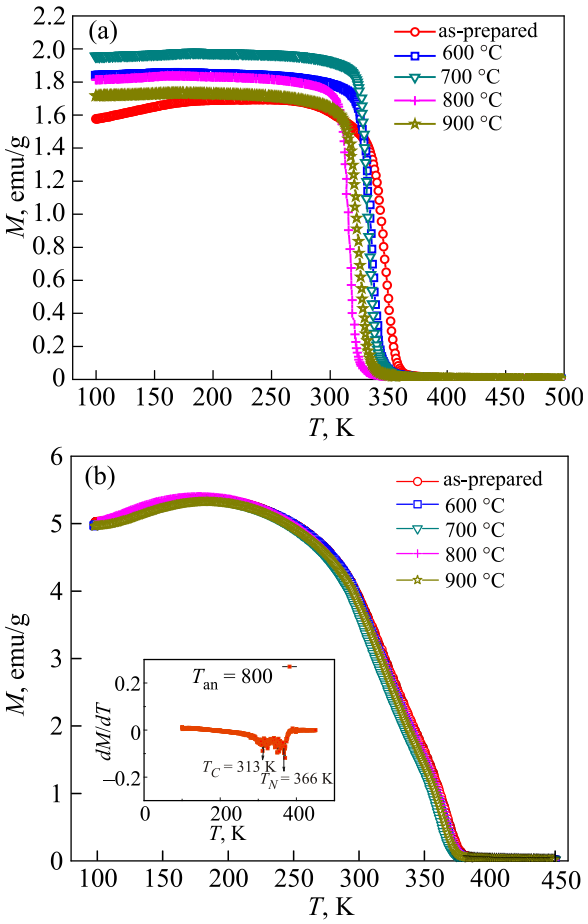

Fig. 7. (Color online) The relation between magnetization and ambient temperature for LBMO (a) and LBMO/NiO (b) (H = 100 Oe), the inset in (b) show dM/dT vs T of T_{an} = 800 °C.

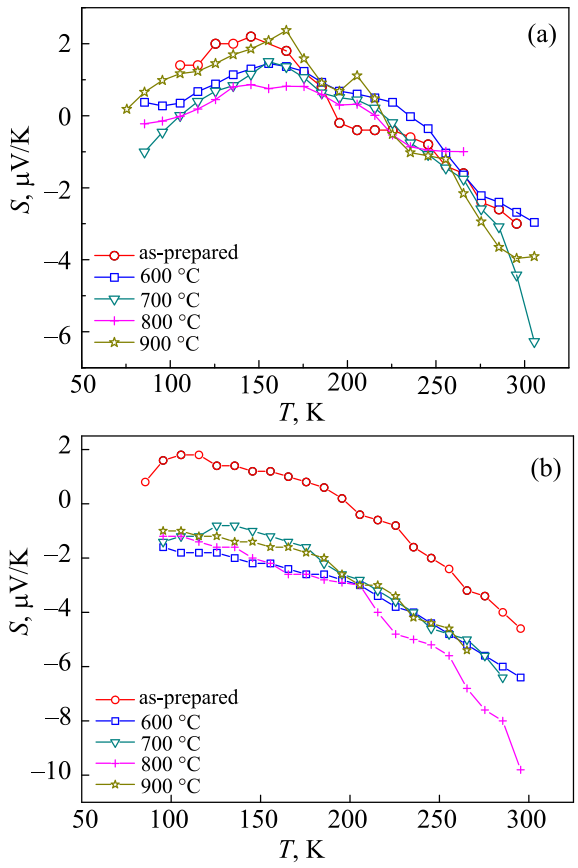

Fig. 8. (Color online) Seebeck coefficient vs ambient temperature for LBMO (a) and LBMO/NiO (b).

It can also be seen that a relatively large difference between T_{ms} and T_C observed for each sample in Table 1, agrees with the difference reported previously [30–32]. The difference is due to the grain boundary that can influence onto T_{ms} shifting it to a lower temperatures [29,30] but does not affect T_C, which is an intrinsic property of the magnetic core of grains. On the other hand, it is observed in Fig. 5 and Fig. 7 that the semiconductor-metal transition occurs when magnetization approaches its maximum value.

3.6. Thermoelectric properties

Thermoelectric properties (TEP) measurement is presented in Fig. 8 depicting the temperature dependence of Seebeck coefficient (S). S shows a crossover from positive to negative sign at a certain temperature T^* that means a contribution of both holes and electrons to conduction. Generally, the annealing treatment of LBMO increases both T^* and T_s, leading to an enhancement of hole conduction (see Table 4). For LBMO/NiO the annealing eliminates T^*. In addition, S of all annealing temperatures has a negative sign which means dominance of electrons conduction. On contrast, T_s (LBMO/NiO) changes unsequentially and shows value smaller than LBMO sample. As in Fig. 8(a), at low temperatures below T_s, S of the annealed samples have absolute values lower than the as-prepared one, while at high temperatures there is a little drag of these values to relatively higher negative values with annealing temperatures (700 and 900 °C). In contrast, S of annealed LBMO/NiO has higher negative values all over the temperature range as in Fig 8(b). The increase in

Table 4. The calculated parameters of $S(T)$ curve, T_s, E_s, T^* and α as function of annealing temperature of LBMO and LBMO/NiO

	Condition T, °C	T_S, K	E_s, mev	T^*, K	α, e/k_B
$x = 0$	As-prepared	265.5	3.19	195	0.01384
	600	275.5	3.07	235	0.01311
	700	265.5	13.87	225	0.05158
	800	215.5	1.97	215	0.00925
	900	255.5	5.32	225	0.02216
$x = 0.1$	As-prepared	195.5	3.45	–	0.01613
	600	165.5	2.78	–	0.01573
	700	175.5	5.29	–	–0.0249
	800	205.5	7.22	–	0.03384
	900	185.5	2.58	–	0.01496

the negative S at high temperatures can be ascribed to Mn^{4+} ions and their dependence on the annealing process [33] that demonstrates the lowest S value for 800 °C annealed sample. At high temperatures, the increase in S has nearly similar trend with resistivity demonstrating the role of DE and scattering mechanism. Activation energy (E_s) is calculated in the semiconducting region from Mott equation $S = \frac{k_B}{e}\left[\frac{E_s}{k_B T} + \alpha\right]$ [18], where α is the polaron kinetic energy-related constant [34]. The E_s values in Table 4 fluctuate with annealing temperatures and have no constant trend for LBMO and LBMO/NiO. In Tables (2), (4) $E_s < E_\rho$ which confirms small polaron conduction [18]. In addition the α values calculated from the Mott equation (Table 4) are smaller than 1 and confirm also the small polaron conduction.

Conclusion

In this work, the structural, magnetic and transport properties of the manganite perovskite LBMO and LBMO/NiO have been investigated. X-ray diffraction analysis shows that our samples crystallize in a rhombohedral structure of as-prepared and annealed samples. Electrical and magnetic properties show that all samples exhibit metallic and ferromagnetic behavior at low temperature ($T < T_{ms}$, T_C) and semiconductor and paramagnetic behavior at high temperature. The negative magnetoresistance of LBMO/NiO was enhanced by the annealing process especially at room temperature from 1.96% for the as-prepared sample to 28.07% for that annealed at 900 °C. If the magnetoresistance response at room temperature can be improved further, it will be a promising candidate for applications in sensors and magnetic recording. The hopping conduction models show that, generally, SPH and VRH conductions coexist in the as-prepared and annealed samples for two compositions. TEP for the as-prepared and annealed samples shows a crossover from positive to negative signal at a certain temperature T^* that means a contribution of both holes and electrons in conduction.

Acknowledgment

Authors acknowledge the finical support provided by the Science and Technology Development Fund (STDF), Egypt, Grant project No 3002.

1. S. Jin, T.H. Tiefel, M. McCormack, R.A. Fastnacht, R. Ramesh, and L.H. Chen, *Science* **264**, 13 (1994).
2. H.L. Ju, J. Gopalakrishnan, J.L. Peng, Q. Li, G.C. Xiong, and R.L. Greene, *Phys. Rev. B* **51**, 6143 (1995).
3. K. Meera,V. Ravindranath, and M. Rao, *J. All. Compd*. **326**, 98 (2001).
4. Y. Cui, R. Wang, and L. Zhang, *J. Appl. Phys*. **103**, 073907 (2008).
5. L. Balcells, A.E. Carrillo, B. Martinesz, and J. Fontcuberta, *Appl. Phys. Lett.* **74**, 4014 (1999).
6. A. Gupta and J.Z. Sun, *J. Magn. Magn. Mater*. **200**, 24 (1999).
7. S. Jin, T.H. Tiefel, M. McCormack, H.M. O'Bryan, L.H. Chen, R. Ramesh, and D. Schurig, *Appl. Phys. Lett.* **67**, 557 (1995).
8. A.M. Ahmed, A.K. Diab, and H.F. Mohamed, *J. Supercond. Nov. Magn*. **24**, 597 (2011).
9. A.M. Ahmed, S.A. Saleh, E.M.M. Ibrahim, and H.F. Mohamed, *J. Magn. Magn. Mater*. **301**, 452 (2006).
10. A.M. Ahmed, *Physica B* **352**, 330 (2004).
11. K. Martin and G. McCarthy, North Dakota State Univ., Frago, ND. USA.ICDD Grant-in- Aid (1991).
12. A. Nossov, J. Pierre, V. Vassiliev, and V. Ustinov, *Solid State Commun*. **101**, 361 (1997).
13. D.C. Shye, C.C. Hwang, M.J. Lai, C.C. Jaing, J.S. Chen, S. Huang, M.H. Juang, B.S. Chiou, and H.C. Cheng, *Jpn. J. Appl. Phys*. **42**, 549 (2003).
14. Yimin Cui, Liuwan Zhang, Chunchang Wang, Kai Shi, and Bisong Cao, *J. Magn. Magn. Mater*. **297**, 21 (2006).
15. P. Dey and T.K. Nath, *Phys. Rev. B* **73**, 214425 (2006).
16. A.P. Ramirez, *J. Phys.: Condens. Matter* **9**, 8171(1997).
17. N. Abdelmoula, A. Cheikh-Rouhou, and L. Reversat, *J. Phys.: Condens. Matter* **13**, 449 (2001).
18. N.F. Mott and E.A. Davis, in: *Electronics Process in Non Cryst. Mater.*, Clarendon Press, Oxford (1979).
19. S. Mollah, H.L. Huang, H.D.Yang, P. Sudipta, S. Taran and B.K. Chaudhuri, *J. Magn. Magn. Mater.* **284**, 383 (2004).
20. M. Viret, L. Ranno, and J.M.D. Coey, *Phys. Rev. B* **55**, 8067 (1997).
21. I.G. Austin and N.F. Mott, *Adv. Phys*. **18**, 41 (1969).
22. S. Mollah, H.L. Huang, H.D. Yang, Sudipta Pal, S. Taran, and B.K. Chaudhuri, *J. Magn. Magn. Mater*. **284**, 383 (2004).
23. T. Holstein, *Ann. Phys*. **8**, 343(1959).
24. A.M. Ahmed, M.A. Abedellateef, H.A. Abd El-Ghanny, and Abd El Mo'ez A. Mohamed, *Phys. Status Solidi A* **212**, 623 (2015).
25. S. Ravi and M. Kar, *Physica B* **348**, 169 (2004).
26. X.J. Liua, Z.Q. Lia, A. Yu, M.L. Liu, W.R. Li, B.L. Li, P. Wu, H.L. Bai, and E.Y. Jiang, *J. Magn. Magn. Mater.* **313**, 360 (2007).
27. S. Othmania, M. Bejar, E. Dhahri, and E.K. Hlil, *J. Alloys Comp.* **475**, 46 (2009).
28. M. Eshraghi, H. Salamati1, and P. Kameli, *J. Phys.: Condens. Matter* **18**, 8281 (2006).
29. D. Alders, L.H. Tjeng, F.C. Voogt, T. Hibma, G.A. Sawatzky, C.T. Chen, J. Vogel, M. Sacchi, and S. Iacobucci, *Phys. Rev. B* **57**, 11623 (1998).
30. A. Dutta, N. Gayathri, and R. Ranganathan, *Phys. Rev. B* **68**, 054432 (2003).
31. G. Venkataiah, and P. Venugopal Reddy, *J. Magn. Magn. Mater.* **285**, 343 (2005).
32. A.M. Ahmed, H.F. Mohamed, A.K. Diab, Abd El Mo'ez A. Mohamed, A.E.A. Mazen, and A.M. Mohamed, *Indian J. Phys.* **89**, 561 (2015).
33. J.A.M. Van Roosmalen, P. van Vlaanderen, and E.H.P. Cordfunke, *J. Solid State Chem*. **114**, 516 (1995).
34. K. Sega, Y. Kuroda, and H. Sakata, *J. Mater. Sci*. **33**, 1303 (1998).